

Using T-Matrix Method for Light Scattering Computations by Non-axisymmetric Particles: Superellipsoids and Realistically Shaped Particles

Thomas Wriedt*

*Dr.-Ing. T. Wriedt, Institut für Werkstofftechnik, Badgasteiner Str. 3, 28359 Bremen (Germany)

tel: +49-421-21-82507, fax: +49-421-218-5378, e-mail: thw@iwt.uni-bremen.de

Abstract

Light scattering by non-axisymmetric particles is commonly needed in particle characterization and other fields. After much work has been devoted to volume discretisation methods to compute scattering by such particles there is renewed interest in the T-matrix method. We extended the *null-field method with discrete sources* for T-matrix computation and implemented the superellipsoid shape using an implicit equation. Additionally a triangular surface patch model of a realistically shaped particle can be used for scattering computations. In this paper some exemplary results of scattering by non-axisymmetric particles will be presented.

Keywords: light scattering, superellipsoid, discrete sources, T-matrix method

1 Introduction

In optical particle characterization, light scattering computations are commonly needed. They help to design new instruments or to investigate the influence of various particle characteristics, such as shape, refractive index, composition or surface roughness on a specific optical particle sizing instrument. Various other parameters of the instrument can also be easily investigated using light scattering simulations. For instance, the effect of the wavelength of the incident laser beam, the effect of particle trajectory through a measurement volume or the influence of the Gaussian intensity distribution of a laser beam can be computed.

There is continuous interest in particle shape characterization. This would help to tell apart e.g. nonspherical particles from spherical ones or fibrous particles from other particles. To develop new instruments for particle shape recognition, of course light scattering theories and corresponding computer programs for nonspherical particles are needed. The different methods available in this field have recently been reviewed by Wriedt [1] and Jones [2]. For this introduction, the various

theories can be divided into volume based ones and surface based theories. Well known volume discretisation methods are the various integral equation methods such as discrete dipole approximation (DDA) [3] and volume integral equation method (VIEM) [4] and the differential equation method finite difference time domain method (FDTD) [5], [6]. Because the whole volume of a scatterer is discretised, computer time is rather high.

Nevertheless, these methods have been applied to compute scattering by nonspherical particles in optical particle sizing and in other fields. Scattering by cubical crystal has been done using DDA [3] and scattering by ice crystal has been investigated using FDTD [5].

Since only the surface of a scattering body is discretised, computer demand should be lower with surface based methods but these methods are not yet that much applied for scattering computation by arbitrarily shaped particles.

The T-matrix method (also called null field method or extended boundary condition method) is the best known of these methods because fast computer codes are easily available [7], [8], but it is mainly applied to scattering by axisymmetric scatterers. The T-matrix method has originally been developed by Waterman in a series of papers [9], [10], [11]. The T-matrix is based on expansion of all fields - the incident, transmitted and the scattered field - into a series of spherical vector wave functions.

A crucial advantage of the null-field method consists in the fact that the transition matrix or the T-matrix relating the scattered and the incident field coefficients can be computed in an easy manner. The T-matrix only depends on the incident wave length and particle shape, its refractive index and its relation to the coordinate system. Thus knowing a T-matrix scattering by a rotated particle, a system of particles, a particle on a plane surface, in incident Gaussian laser beam and orientation averaged scattering can easily be computed.

Taking into account the general properties of the T-matrix Mishchenko has elaborated an efficient analytical method for computing orientationally-averaged light scattering characteristics for ensembles of nonspherical particles [12]. On the other hand, the T-matrix for a single scatterer can successfully be used for solving a large class of boundary-value problems in electromagnetic scattering theory. In this context, we mention the analysis of multiple scattering problems [13],[14] simulation of light scattering by layered or composite objects [15], [16], [17] and by particles deposited upon a surface [18].

However, for particles with extreme geometries or particles with appreciable concavities the single spherical coordinate based null-field method fails to converge. A number of modifications to the

conventional null-field method have been suggested to improve the numerical stability. These techniques include formal modifications of the single-spherical-coordinate-based null-field method [19], [20], [21], different choices of basis functions [22], [23] and the application of the spheroidal coordinate formalism [24], [25]. One of these formal modifications is the *null-field method with discrete sources* [26], [27], [28]. Essentially, this method entails the use of a number of elementary sources for approximating the surface current densities. The discrete sources are placed on a certain support in an additional region with respect to the region where the solution is required. Unknown discrete sources amplitudes which produce the surface densities are computed by using the null-field condition of the total electric field inside the particle surface. With this method, scattering computation by highly elongated or flat scatterers such as fibres and plates [29] and layered particles [30] are easily possible and the standard T-matrix can also be computed [31] for postprocessing such as cluster scattering or orientation averaging.

Some brief comments on the history of T-matrix method for non-axisymmetric particles may be of interest. Early scattering computation for non-axisymmetric scatterers using the T-matrix method have been done by *P. W. Barber* in his PhD Thesis [32] and by *Schneider* [33], both presenting results for ellipsoids.

The *null field method with discrete sources* has also been extended for scattering computation by non-axisymmetric scatterers [34] and the method has been fully tested by comparison to other methods [35] giving results for cubes.

A 3D variant of the T-matrix method has also been developed by *Laitinen et al* [36] and by *Kahnert et al.* [37] both presenting scattering results for rounded cubes and another one by *Havemann et al.* [38] giving results for hexagonal icecrystals.

To describe the scattering body using smooth functions *Laitinen et al* [36] expand the surface of the scattering cube into a series of spherical harmonics. The problem with this method is that artificial roughness is introduced with this method in addition to rounding of the edges of the cube.

In optical particle characterization, mainly scattering computation by some basic particle shapes have been investigated such as spheres, spheroids, ellipsoids, cubes and finite cylinders. Because there is a lack of tools to describe particle shape in the following the superellipsoid is proposed to generate various interesting particle shapes and it is integrated into the *null field method with discrete sources*.

The concept of the paper is arranged as follows. First the superellipsoid particle shape will be described; next the *null field method with discrete sources* will shortly be introduced and finally

some examples of computational results will be presented.

2 Superellipsoid

The superellipsoid represents a family of 3-dimensional shapes by a product of two superquadratic curves [40]. This shape is well known in computer graphics and it can be used to model a wide range of shapes such as spheres, ellipsoids and cylinders and especially cubes and cylinders with rounded edges [39]. The superellipsoid is implemented in various computer programs used in computer graphics such as POV-Ray, so that a visualization of its form is easily available. The superellipsoid or superquadratic ellipsoid might be considered a generalization of the ellipsoid, and its implicit form is given by the following equation

$$[(x/a)^{2/e} + (y/b)^{2/e}]^{e/n} + (z/c)^{2/n} - 1 = 0. \quad (1)$$

We are using the same nomenclature as in POV-Ray.

n is the north-south roundedness and e is the east-west roundedness and the bounds in x, y, z are given by the parameters a, b, c .

The parametric form of the equation may also be useful in the construction of an object. The parametric equation of the superellipsoid is given by

$$\begin{aligned} x &= a \cos^n(\vartheta) \cos^e(\varphi) \\ y &= b \cos^n(\vartheta) \sin^e(\varphi) \\ z &= c \sin^n(\vartheta) \\ \vartheta &: [-\pi/2, \pi/2], \varphi : [-\pi, \pi]. \end{aligned} \quad (2)$$

If n and e are not equal to 1 the angles ϑ, φ off cause no longer correspond to the coordinates of the spherical coordinate system. A problem would arise in the equation if $\cos(t)$ or $\sin(t)$ was negative. In this case a negative number could have a fractional exponent, which is an illegal operation. Therefore the interpretation, that $(t)^p$ has the same sign as t and the same magnitude as $|t|^p$ is adopted by using the following operator.

$$(t)^p = \text{sign}(t) |t|^p. \quad (3)$$

| | | | | | | |
|--------|--------|------------|------------|------------|------------|------------|
| e, n | 0 | 0.2 | 0.5 | 0.7 | 1.0 | 2.0 |
| V | $8abc$ | $7.675abc$ | $6.482abc$ | $5.538abc$ | $4.189abc$ | $1.333abc$ |

Table 1: Volume of some exemplary superellipsoids

To produce only convex shapes the values for n and e would be bounded: $0 < \{n, e\} < 2$. To prevent numerical overflow and difficulties with singularities it is advisable to use a further bound: $0.1 < \{n, e\} < 1.9$. The variety of particle shapes, which can be modelled using the superellipsoid equation, is plotted in Fig. 1.

The variables n and e are varied between 0.2 and 2.0, whereas the bounds a, b, c are kept constant. One can see that a variety of shapes from sphere, rounded cube, circular or rectangular cylinder, octahedra up to even some star shaped objects can be generated.

The volume of a superellipsoid can be computed from [40]:

$$V = 2 a b c n e B\left(\frac{n}{2}, n\right) B\left(\frac{e}{2}, \frac{e}{2}\right). \quad (4)$$

The term $B(x, y)$ is the beta function which is related to the gamma function:

$$B(x, y) = 2 \int_0^{\pi/2} \sin^{2x-1} \phi \cos^{2y-1} \phi d\phi = \frac{\Gamma(x) \Gamma(y)}{\Gamma(x+y)}. \quad (5)$$

The volume of some exemplary superellipsoids is given in table Tab. 1:

For the exemplary computation in the following section the rounded cube shapes depicted in Fig. 2 will be used. The parameters n and e are 0.2; 0.5; 0.7 such that cubes with a different roundedness result.

3 Null-field Method with Discrete Sources

In this section we would like to outline the basics of the *null-field method with discrete sources* [28]. Let us consider a three-dimensional space D consisting of the union of a closed surface S , its interior D_i and its exterior D_s . We denote by k_t the wave number in the domain D_t , where $k_t = k\sqrt{\epsilon_t\mu_t}$, $k = \omega/c$ and $t = s, i$.

The transmission boundary-value problem can be formulated as follows. Let $\mathbf{E}_0, \mathbf{H}_0$ be an entire solution to the Maxwell equations representing an incident electromagnetic field. Find the vector

fields, $\mathbf{E}_s, \mathbf{H}_s \in C^1(D_s) \cap C(\overline{D_s})$ and $\mathbf{E}_i, \mathbf{H}_i \in C^1(D_i) \cap C(\overline{D_i})$ satisfying the Maxwell's equations

$$\nabla \times \mathbf{E}_t = jk\mu_t \mathbf{H}_t, \quad (6)$$

$$\nabla \times \mathbf{H}_t = -jk\varepsilon_t \mathbf{E}_t,$$

in D_t , where $t = s, i$, and two boundary conditions:

$$\mathbf{n} \times \mathbf{E}_i - \mathbf{n} \times \mathbf{E}_s = \mathbf{n} \times \mathbf{E}_0, \quad (7)$$

$$\mathbf{n} \times \mathbf{H}_i - \mathbf{n} \times \mathbf{H}_s = \mathbf{n} \times \mathbf{H}_0,$$

on S . In addition, the scattered field $\mathbf{E}_s, \mathbf{H}_s$ must satisfy the Silver-Müller radiation condition uniformly for all directions \mathbf{x}/x . It is known that the transmission boundary-value problem possesses an unique solution [41].

For solving the transmission boundary-value problem in the framework of the null-field method with discrete sources the scattering object is replaced by a set of surface current densities \mathbf{e} and \mathbf{h} , so that in the exterior domain the sources and fields are exactly the same as those existing in the original scattering problem. The entire analysis can conveniently be broken down into the following three steps:

(I) A set of integral equations for the surface current densities \mathbf{e} and \mathbf{h} is derived for a variety of discrete sources. Physically, the set of integral equations in question guarantees the null-field condition within D_i . It is noted that localized and distributed vector spherical functions, magnetic and electric dipoles or vector Mie-potentials can be used as discrete sources. Essentially, the null-field method with discrete sources consists in the projection relations:

$$\int_S^{\square} (\mathbf{e} - \mathbf{e}_0) \cdot \Psi_\nu^3 + j \sqrt{\frac{\mu_s}{\varepsilon_s}} (\mathbf{h} - \mathbf{h}_0) \cdot \Phi_\nu^3 \Big] dS = 0 \quad (8)$$

$$\int_S^{\square} (\mathbf{e} - \mathbf{e}_0) \cdot \Phi_\nu^3 + j \sqrt{\frac{\mu_s}{\varepsilon_s}} (\mathbf{h} - \mathbf{h}_0) \cdot \Psi_\nu^3 \Big] dS = 0, \quad \nu = 1, 2, \dots$$

where $\mathbf{e}_0 = \mathbf{n} \times \mathbf{E}_0$ and $\mathbf{h}_0 = \mathbf{n} \times \mathbf{H}_0$ are the tangential components of the incident electric and magnetic fields. The set $\{\Psi_\nu^3, \Phi_\nu^3\}_{\nu=1,2,\dots}$ consists of radiating solutions to Maxwell equations and depends on the system of discrete sources which is used for imposing the null-field condition. Actually, this set together with the set of regular solutions to Maxwell equations $\{\Psi_\nu^1, \Phi_\nu^1\}_{\nu=1,2,\dots}$ stands for

- localized vector spherical functions $\left\{ \mathbf{M}_{mn}^{1,3}, \mathbf{N}_{mn}^{1,3} \right\}_{m \in \mathbf{Z}, n \geq \max(1, |m|)}$,

$$\begin{aligned} \mathbf{M}_{mn}^{1,3}(k\mathbf{x}) &= \sqrt{D_{mn}} z_n(kr) \left[jm \frac{P_n^{|m|}(\cos \theta)}{\sin \theta} \mathbf{e}_\theta - \frac{dP_n^{|m|}(\cos \theta)}{d\theta} \mathbf{e}_\varphi \right] e^{jm\varphi}, \\ \mathbf{N}_{mn}^{1,3}(k\mathbf{x}) &= \sqrt{D_{mn}} \left\{ n(n+1) \frac{z_n(kr)}{kr} P_n^{|m|}(\cos \theta) e^{jm\varphi} \mathbf{e}_r \right. \\ &\quad \left. + \frac{[kr z_n(kr)]'}{kr} \left[\frac{dP_n^{|m|}(\cos \theta)}{d\theta} \mathbf{e}_\theta + jm \frac{P_n^{|m|}(\cos \theta)}{\sin \theta} \mathbf{e}_\varphi \right] \right\} e^{jm\varphi}, \end{aligned} \quad (9)$$

where $(\mathbf{e}_r, \mathbf{e}_\theta, \mathbf{e}_\varphi)$ are the unit vectors in spherical coordinates, z_n designates the spherical Bessel functions j_n or the spherical Hankel functions of the first kind h_n^1 , $P_n^{|m|}$ denotes the associated Legendre polynomial of order n and m , and D_{mn} is a normalization constant given by

$$D_{mn} = \frac{2n+1}{4n(n+1)} \cdot \frac{(n-|m|)!}{(n+|m|)!}, \quad (10)$$

- distributed vector spherical functions $\left\{ \mathcal{M}_{mn}^{1,3}, \mathcal{N}_{mn}^{1,3} \right\}_{m \in \mathbf{Z}, n=1,2,\dots} :$

$$\begin{aligned} \mathbf{M}_{mn}^{1,3}(k\mathbf{x}) &= \mathbf{M}_{m,|m|+l}^{1,3}(k(\mathbf{x}-z_n\mathbf{e}_3)), \mathbf{x} \in \mathbf{R}^3 - \{z_n\mathbf{e}_3\}_{n=1}^\infty, \\ \mathcal{N}_{mn}^{1,3}(k\mathbf{x}) &= \mathbf{N}_{m,|m|+l}^{1,3}(k(\mathbf{x}-z_n\mathbf{e}_3)), \mathbf{x} \in \mathbf{R}^3 - \{z_n\mathbf{e}_3\}_{n=1}^\infty, \end{aligned} \quad (11)$$

where $m \in \mathbf{Z}$, $n = 1, 2, \dots$, $l = 1$ if $m = 0$ and $l = 0$ if $m \neq 0$, and $\{z_n\}_{n=1}^\infty$ is a set of points located on a segment Γ_z of the z -axis,

- magnetic and electric dipoles $\left\{ \mathcal{M}_{ni}^{1,3}, \mathcal{N}_{ni}^{1,3} \right\}_{n=1,2,\dots, i=1,2} :$

$$\begin{aligned} \mathcal{M}_{ni}^{1,3}(k\mathbf{x}) &= \mathbf{m}(\mathbf{x}_n^\pm, \mathbf{x}, \tau_{ni}^\pm), \mathbf{x} \in \mathbf{R}^3 - \{\mathbf{x}_n^\pm\}_{n=1}^\infty, \\ \mathcal{N}_{ni}^{1,3}(k\mathbf{x}) &= \mathbf{n}(\mathbf{x}_n^\pm, \mathbf{x}, \tau_{ni}^\pm), \mathbf{x} \in \mathbf{R}^3 - \{\mathbf{x}_n^\pm\}_{n=1}^\infty, \end{aligned} \quad (12)$$

where $n = 1, 2, \dots, i = 1, 2$, τ_{n1} and τ_{n2} are two tangential linear independent unit vectors at the point \mathbf{x}_n ,

$$\mathbf{m}(\mathbf{x}, \mathbf{y}, \mathbf{a}) = \frac{1}{k^2} \mathbf{a}(\mathbf{x}) \times \nabla_{\mathbf{y}} g(\mathbf{x}, \mathbf{y}, k), \quad \mathbf{n}(\mathbf{x}, \mathbf{y}, \mathbf{a}) = \frac{1}{k} \nabla_{\mathbf{y}} \times \mathbf{m}(\mathbf{x}, \mathbf{y}, \mathbf{a}), \quad \mathbf{x} \neq \mathbf{y}, \quad (13)$$

and the sequence $\{\mathbf{x}_n^-\}_{n=1}^\infty$ is dense on a smooth surface S^- enclosed in D_i , while the sequence $\{\mathbf{x}_n^+\}_{n=1}^\infty$ is dense on a smooth surface S^+ enclosing D_i , or finally for the set of

- vector Mie-potentials $\left\{ \mathcal{M}_n^{1,3}, \mathcal{N}_n^{1,3} \right\}_{n=1,2,\dots}$:

$$\begin{aligned} \mathcal{M}_n^{1,3}(k\mathbf{x}) &= \frac{1}{k} \nabla \times (\varphi_n^\pm(\mathbf{x})\mathbf{x}), \quad \mathbf{x} \in \mathbf{R}^3 - \{\mathbf{x}_n^\pm\}_{n=1}^\infty, \\ \mathcal{N}_n^{1,3}(k\mathbf{x}) &= \frac{1}{k} \nabla \times \mathcal{M}_n^{1,3}(k\mathbf{x}), \quad \mathbf{x} \in \mathbf{R}^3 - \{\mathbf{x}_n^\pm\}_{n=1}^\infty, \end{aligned} \quad (14)$$

where the Green functions

$$\varphi_n^\pm(\mathbf{x}) = g(\mathbf{x}_n^\pm, \mathbf{x}, k), \quad n = 1, 2, \dots$$

have singularities $\{\mathbf{x}_n^-\}_{n=1}^\infty$ and $\{\mathbf{x}_n^+\}_{n=1}^\infty$ distributed on the auxiliary surfaces S^- and S^+ , respectively. By convention, when we refer to the null-field equations (8) we implicitly refer to all equivalent forms of these equations.

(II) The surface current densities are approximated by fields of discrete sources. In this context let \mathbf{e} and \mathbf{h} solve the null-field equations (8) and assume that the system $\{\mathbf{n} \times \Psi_\mu^1, \mathbf{n} \times \Phi_\mu^1\}_{\mu=1}^\infty$ form a Schauder basis in $\mathcal{L}_{\text{tan}}^2(S)$. Then there exists a sequence $\{a_\mu, b_\mu\}_{\mu=1}^\infty$ such that

$$\begin{aligned} \mathbf{e}(\mathbf{y}) &= \sum_{\mu=1}^\infty a_\mu \mathbf{n} \times \Psi_\mu^1(k_i \mathbf{y}) + b_\mu \mathbf{n} \times \Phi_\mu^1(k_i \mathbf{y}), \quad \mathbf{y} \in S, \\ \mathbf{h}(\mathbf{y}) &= -j \sqrt{\frac{\varepsilon_i}{\mu_i}} \sum_{\mu=1}^\infty a_\mu \mathbf{n} \times \Phi_\mu^1(k_i \mathbf{y}) + b_\mu \mathbf{n} \times \Psi_\mu^1(k_i \mathbf{y}), \quad \mathbf{y} \in S. \end{aligned} \quad (15)$$

We recall that a system $\{\psi_i\}_{i=1}^\infty$ is called a Schauder basis of a Banach space X if any element $u \in X$ can be uniquely represented as $u = \sum_{i=1}^\infty \alpha_i \psi_i$, where the convergence of the series is in the norm of X . It is noted that in the case of localized vector spherical functions the notion of Schauder basis is closely connected with the Rayleigh hypothesis. This hypothesis says that the series representation of the scattered field in terms of radiating localized vector spherical functions, which uniformly converges outside the circumscribing sphere, also converges on S .

(III) Once the surface current densities are determined the scattered field outside the circumscribing sphere is obtained by using the representation theorem. We get the series representation

$$\mathbf{E}_s(\mathbf{x}) = \sum_{\nu=1}^\infty f_\nu \mathbf{M}_\nu^3(k_s \mathbf{x}) + g_\nu \mathbf{N}_\nu^3(k_s \mathbf{x}), \quad (16)$$

where

$$\begin{aligned} f_\nu &= \frac{jk_s^2}{\pi} \int_S^\square \left[\mathbf{e}(\mathbf{y}) \cdot \mathbf{N}_{\bar{\nu}}^1(k_s \mathbf{y}) + j \sqrt{\frac{\mu_s}{\varepsilon_s}} \mathbf{h}(\mathbf{y}) \cdot \mathbf{M}_{\bar{\nu}}^1(k_s \mathbf{y}) \right] dS(\mathbf{y}), \\ g_\nu &= \frac{jk_s^2}{\pi} \int_S^\square \left[\mathbf{e}(\mathbf{y}) \cdot \mathbf{M}_{\bar{\nu}}^1(k_s \mathbf{y}) + j \sqrt{\frac{\mu_s}{\varepsilon_s}} \mathbf{h}(\mathbf{y}) \cdot \mathbf{N}_{\bar{\nu}}^1(k_s \mathbf{y}) \right] dS(\mathbf{y}). \end{aligned} \quad (17)$$

Here, $\bar{\nu}$ is a complex index incorporating $-m$ and n , i.e. $\bar{\nu} = (-m, n)$.

3.1 T-matrix Computation

Now, for deriving the T-matrix let us assume that the incident field can be expressed inside a finite region containing S as a series of regular vector spherical functions

$$\begin{aligned} \mathbf{E}_0(\mathbf{x}) &= \sum_{\nu=1}^{\infty} a_\nu^0 \mathbf{M}_\nu^1(k_s \mathbf{x}) + b_\nu^0 \mathbf{N}_\nu^1(k_s \mathbf{x}), \\ \mathbf{H}_0(\mathbf{x}) &= -j \sqrt{\frac{\varepsilon_s}{\mu_s}} \sum_{\nu=1}^{\infty} a_\nu^0 \mathbf{N}_\nu^1(k_s \mathbf{x}) + b_\nu^0 \mathbf{M}_\nu^1(k_s \mathbf{x}). \end{aligned} \quad (18)$$

Then, using (8)-(18) we see that the relation between the scattered and the incident field coefficients is linear and is given by a transition matrix \mathbf{T} as follows

$$\begin{bmatrix} f_\nu \\ g_\nu \end{bmatrix} = \mathbf{T} \begin{bmatrix} a_\nu^0 \\ b_\nu^0 \end{bmatrix}. \quad (19)$$

Here

$$\mathbf{T} = \mathbf{B} \mathbf{A}^{-1} \mathbf{A}_0, \quad (20)$$

where \mathbf{A} , \mathbf{B} and \mathbf{A}_0 are block matrices written in general as

$$\mathbf{X} = \begin{bmatrix} X_{\nu\mu}^{11} & X_{\nu\mu}^{12} \\ X_{\nu\mu}^{21} & X_{\nu\mu}^{22} \end{bmatrix}, \quad \nu, \mu = 1, 2, \dots, \quad (21)$$

with \mathbf{X} standing for \mathbf{A} , \mathbf{B} and \mathbf{A}_0 . Explicit expressions for the elements of these matrices are given in appendix A.

It is noted that the exact infinite T-matrix is independent of the expansion systems used on S . However, the approximate truncated matrix, computed according to

$$\mathbf{T}_N = \mathbf{B}_N \mathbf{A}_N^{-1} \mathbf{A}_{0N} \quad (22)$$

does contain such a dependence.

Energy characteristics in the far field are computed from the far-field pattern \mathbf{E}_{s0}^N for an unit amplitude incident electric field for p- or s-polarization. The angle-dependent intensity function plotted in the simulation section is the normalized differential scattering cross-section (DSCS)

$$\frac{\sigma_d}{\pi a^2} = \frac{|k_s \mathbf{E}_{s0}^N|^2}{\pi |k_s a|^2}. \quad (23)$$

To numerically compute orientation averaged scattering three integrals with respect to the three Euler α, β, γ angles have to be computed. Thus the value of interest $f(\alpha, \beta, \gamma)$ is integrated over all directions and polarization of the incident plane wave. The numerical procedure used to do this is based on a step wise procedure

$$\int_0^{2\pi} \int_0^\pi \int_0^{2\pi} f(\alpha, \beta, \gamma) d\alpha \sin \beta d\beta d\gamma \approx \sum_{n_\alpha=1}^{N_\alpha} \sum_{n_\beta=1}^{N_\beta} \sum_{n_\gamma=1}^{N_\gamma} f(\alpha, \beta, \gamma) \sin(n_\beta \pi / N_\beta) \frac{n_\alpha 2\pi n_\beta \pi n_\gamma 2\pi}{N_\alpha N_\beta N_\gamma}. \quad (24)$$

The triple integral is converted to three summations. Angle α is digitized for N_α steps in the range $(0, 2\pi)$, angle β is digitized for N_β steps in the range $(0, \pi)$, and angle γ is digitized for N_γ steps in the range $(0, 2\pi)$.

4 Mesh Generation

Implicit surfaces are commonly used for modelling purposes in numerous scientific applications, including CAD system and computer graphics. Therefore there are various interests in constructing a polyhedral representation of implicit surfaces [42]. In our case the representation in a triangular patch model should allow firstly a correct calculation of surface integrals and secondly a graphical visualization of the particle. Different methods are available to create a geometric surface mesh.

To generate the superellipsoid shape for our light scattering simulations we are using the *HyperFun* software tool [43], [44] which is a program supporting high-level language functional representations in computer graphics. Function representation is a generalization of traditional implicit surfaces and constructive solid geometry which allows construction of quite complex shapes such as isosurfaces of real-valued functions composed of functionally defined primitives and operations [45]. The *HyperFun*

polygonizer used for surface mesh generation generates VRML output of a triangular patch model. *HyperFun* generates a sufficiently regular mesh which, although intended for computer graphics, is very well suited for our application as we found.

An example of gridding is shown with the rounded cubes given in Fig. 2. In these examples the dimensions are $a = b = c = 0.3\mu\text{m}$ and the number of triangular patches are 1448, 1448, 1400.

In the standard method to compute surface integrals the parametric equation is used and thus an equivalent integral in planar coordinates has to be evaluated. Thus partial derivatives of x, y, z with respect to the parametrization (in our case parameters ϑ, φ) are needed which may not be available analytically. If the partial derivatives are not available a numerical method via finite differences may be used.

We use an alternative approach based on a modified centroid quadrature that does not use the partial derivatives. This modified centroid quadrature has been proposed and investigated by Georg and Tauch [46]. The surface integrals to be computed are approximated by

$$\int_S f dS \approx \sum_i f(v_{i,c}) \text{area}[v_{i,1}, v_{i,2}, v_{i,3}] . \quad (25)$$

Here, $v_{i,1}, v_{i,2}, v_{i,3}$ are the vertices spanning a triangle and point $v_{i,c}$ denotes the centre of mass of the triangle $[v_{i,1}, v_{i,2}, v_{i,3}]$ given by

$$v_{i,c} = \frac{1}{3} \sum_{j=1}^3 v_{i,j} . \quad (26)$$

Thus the integral over each triangle is approximated by multiplying the value of the integrand at the centroid by the triangle area.

5 Numerical Simulations

5.1 Program Validation

The computer program based on the DSM theory has been checked using various internal checks such as computing scattering by a shifted particle and comparing the result to scattering by the original particle.

Next the program has been validated by comparing to other programs. We used the T-Matrix programs t1 included with the book by *Barber and Hill* [7]. The first result is for a spheroid with dimensions of $a = b = 500nm, c = 700nm$. Practically no difference has been found, as can be seen by the normalized DSCS for p- and s-polarization plotted in Fig. 3. The T-Matrix result is shifted versus the DSM result because Barber and Hill apply a different normalization in the differential scattering cross section (DSCS) computed. To check the routine for orientation averaging the program t5 of *Barber and Hill* [7] is used to compute a reference result of the orientation averaged DSCS for the same spheroid. The results of both computations are plotted in Fig. 4 and there is perfect agreement between the results computed by the DSM program and the t5 programm.

As another example for program validation scattering by an ellipsoid with dimensions $a = 150, b = 200, c = 300nm$ will be presented in Fig. 5. The comparative result of the DSCS has been computed with another implementation of the same theory [47]. As can be seen there is perfect agreement between both results.

To present a final example of program validation for non-axisymmetric particles the 3D-Multiple Multipole Program (MMP) of *Hafner and Bomholt* [48] was used for computation of a scattering result of a rounded cube to compare with. This method is based on an expansion of the internal and the scattered field into so called multipoles. A generalized point matching method is used to fulfill the boundary conditions on the surface of the scattering particle and to compute the coefficients of the expansion functions. In the example given we used spherical vector wave functions for field expansion. The FORTRAN code is available with the MMP book and this code has been modified such that a triangular surface patch model of the scattering particle could be read into the program to be used for the point matching procedure. As mirror symmetry can be accounted for in the MMP program only an eighths of the surface of the rounded cube has to be used for triangulation into a triangular surface patch model. In the example presented this surface was covered by 1435 faces. The rounded cube was generated by the superellipsoid equation with the following parameters $e = n = 0.2; a = b = c = 2.0\mu m$. The computational results of the differential scattering cross section are plotted in Fig. 6 and Fig. 7. Apart from some different normalization of the DSCS there is almost perfect agreement between the MMP and the DSM result.

| N_{\max} | M_{\max} | MN_{\max} |
|------------|------------|-------------|
| 20 | 18 | 434 |
| 22 | 20 | 522 |
| 25 | 25 | 726 |

Table 2: Number of expansion functions

5.2 Convergence

A profound convergence test is an important step in program testing. Two kinds of convergence checks have to be made a) versus the number of triangular faces of the particles, corresponding to the number of integration elements and b) versus the number of localized spherical vector wave functions used for field expansion. Fig. 8 shows an exemplary result for a convergence test versus the number of integration elements (faces) for a rounded cube with parameters $a = 300nm$, $n = e = 0.2$ and refractive index of $M = 1.5$. By comparing the curves it can be seen that convergence is easily reached and from further investigation we conclude that convergence versus the number of integration elements seems to be mainly uncritical and can easily be achieved. Of more importance is a convergence check versus the number of expansion functions. This number depends on the maximum value of the indices n and m (N_{\max} and M_{\max}) of the spherical vector wave functions $\mathbf{M}_{\vec{n}}$ and $\mathbf{N}_{\vec{n}}$. This number of expansion functions MN_{\max} is given by

$$MN_{\max} = N_{\max} + M_{\max}(2N_{\max} - M_{\max} + 1) . \quad (27)$$

This corresponds to a size of the transition matrix given by $\mathbf{T}(2MN_{\max}, 2MN_{\max})$. Various convergence checks have been done to test the program for different shapes of scatterers. An exemplary result of such a convergence test is given in Fig. 9 where the differential scattering cross section is plotted for a cube. The values of the parameters N_{\max} and M_{\max} used in the simulation and the resulting corresponding number of expansion functions MN_{\max} is summarized in table Tab. 2

5.2.1 Scattering by Rounded Cube

In the following section some sample results of single scattering by the superellipsoids pictured in Fig. 2 will be presented.

Fig. 10 and Fig. 11 give the differential scattering cross section of a cube with dimensions $a = b = c = 1.5\mu m$ and different values of the two roundedness parameters. The first figure gives p-polarization and the second s-polarization.

Scattering by even larger rounded cubes is plotted in the next figures. Fig. 12 and Fig. 13 give the differential scattering cross section of a cube with dimensions and different values of the two roundedness parameters. The influence of roundedness is especially seen in p-polarization at a scattering angle of 45 to 90 degrees.

Just a single exemplary scattering result for orientation averaged scattering by a rounded cube with roundedness parameters $e, n = 0.5$ is given in Fig. 14. p- and s-polarization results almost become indistinguishable and the angular variation in the DSCS is much smoother than that for the same particle in a fixed orientation.

5.2.2 Scattering by Realistically Shaped Particles

To demonstrate that scattering by an arbitrarily shaped particle is also possible with the program developed, the shape of asteroid KY26 was used. Its shape is available as a triangular surface patch model in the wavefront format in the internet [49]. There are 4092 faces in the data file and the dimension of the 0.030km asteroid was scaled down by a factor of $100\mu\text{m}/\text{km}$ such that a particle with a range of $2.92\mu\text{m}$ in x , $2.65\mu\text{m}$ in y and $2.77\mu\text{m}$ in z resulted. Three different views of this KY26 shaped particle are given in Fig. 15. The number of triangular faces was increased to 16.368 using a one-to-four triangular subdivision scheme. In Fig. 16 the differential scattering cross section is plotted. As orientation the orientation given in the original data file is used with z being the direction of the incident plane wave. In Fig. 17 the orientation averaged differential scattering cross section is given. It can be seen that the angular variation in the DSCS is smoother than that computed for the same particle in a fixed orientation.

To demonstrate that scattering from realistically shaped particles can be computed a number of photos from a pebble from different views were used to reconstruct a realistic particle shape. Similarly electron micrography from different views of a small particle could be used to reconstruct its 3D shape. The geometry of the pebble was reconstructed from an image sequence of apparent contour profiles from 20 different viewpoints taken by an electronic camera [50].

Three views of the reconstructed realistically shaped particle are shown in Fig. 18. The dimensions of the particle were scaled such that its size in x is $2.176\mu\text{m}$ in y is 1.585 and in z is $1.856\mu\text{m}$. The shape of the particle was triangulated with 27745 faces. In Fig. 19 the orientation averaged differential scattering cross section of this particle is plotted.

To generate an arbitrarily shaped particle with a different amount of surface roughness the DOS

program PovRockGen [51] was used. The dimensions of the particles generated are such that its overall size in x is $2.026\mu\text{m}$ in y is 2.026 and in z is $1.969\mu\text{m}$. The parameters to generate the smooth particle are $\text{depth}=4$, $\text{smoothness}=2.0$ the parameters to generate the rough particle are $\text{depth}=4$, $\text{smoothness}=1.5$. Originally 5120 surface triangles were generated. These were increased to 20480 by an one-to-four triangular subdivision scheme.

The two different kinds of particle shapes generated and used for scattering computations are shown in Fig. 20 and the orientation averaged computation results are plotted in Fig. 21. With the smooth particle oscillations in the scattering diagram are more pronounced. With the rougher particle the amount of cross polarization is ofcourse increased.

6 Conclusions

An efficient way for computing scattering by non-axisymmetric particles in the framework of the *null-field method with discrete sources* has been presented. The superellipsoid has been introduced to represent a wide range of realistic particle shapes. Additionally reading a triangular surface patch model of a scattering particle has been implemented in the computational procedure.

Numerical experiments have been performed for superellipsoids representing a rounded dielectric cube and some realistically shaped particles. It has been demonstrated that this method is very well suited to compute the T-matrix for non-axisymmetric particles with an over all dimension of $4\mu\text{m}$ with a desktop computer. A Windows 9X program including graphical user interface for computing scattering by superellipsoid is available from our web site [52].

The program has mainly been developed to investigate the effect of particle shape with various kind of methods and instruments in optical particle characterization such as intensity based optical particle counters, intensity ratioing technique, visibility technique, Phase Doppler Anemometry, diffraction type of instruments, static light scattering etc.

7 Appendix

The block elements of matrices \mathbf{A} , \mathbf{B} and \mathbf{A}_0 are given by

$$\begin{aligned}
 A_{\nu\mu}^{11} &= \int_S [(\mathbf{n} \times \Psi_\mu^1) \cdot \Psi_\nu^3 + M(\mathbf{n} \times \Phi_\mu^1) \cdot \Phi_\nu^3] dS, \\
 A_{\nu\mu}^{12} &= \int_S [(\mathbf{n} \times \Phi_\mu^1) \cdot \Psi_\nu^3 + M(\mathbf{n} \times \Psi_\mu^1) \cdot \Phi_\nu^3] dS, \\
 A_{\nu\mu}^{21} &= \int_S [(\mathbf{n} \times \Psi_\mu^1) \cdot \Phi_\nu^3 + M(\mathbf{n} \times \Phi_\mu^1) \cdot \Psi_\nu^3] dS, \\
 A_{\nu\mu}^{22} &= \int_S [(\mathbf{n} \times \Phi_\mu^1) \cdot \Phi_\nu^3 + M(\mathbf{n} \times \Psi_\mu^1) \cdot \Psi_\nu^3] dS,
 \end{aligned} \tag{28}$$

$$\begin{aligned}
 B_{\nu\mu}^{11} &= \frac{jk_s^2}{\pi} \int_S [(\mathbf{n} \times \Psi_\mu^1) \cdot \mathbf{N}_\nu^1 + M(\mathbf{n} \times \Phi_\mu^1) \cdot \mathbf{M}_\nu^1] dS, \\
 B_{\nu\mu}^{12} &= \frac{jk_s^2}{\pi} \int_S [(\mathbf{n} \times \Phi_\mu^1) \cdot \mathbf{N}_\nu^1 + M(\mathbf{n} \times \Psi_\mu^1) \cdot \mathbf{M}_\nu^1] dS, \\
 B_{\nu\mu}^{21} &= \frac{jk_s^2}{\pi} \int_S [(\mathbf{n} \times \Psi_\mu^1) \cdot \mathbf{M}_\nu^1 + M(\mathbf{n} \times \Phi_\mu^1) \cdot \mathbf{N}_\nu^1] dS, \\
 B_{\nu\mu}^{22} &= \frac{jk_s^2}{\pi} \int_S [(\mathbf{n} \times \Phi_\mu^1) \cdot \mathbf{M}_\nu^1 + M(\mathbf{n} \times \Psi_\mu^1) \cdot \mathbf{N}_\nu^1] dS,
 \end{aligned} \tag{29}$$

and

$$\begin{aligned}
 A_{0\nu\mu}^{11} &= \int_S [(\mathbf{n} \times \mathbf{M}_\mu^1) \cdot \Psi_\nu^3 + (\mathbf{n} \times \mathbf{N}_\mu^1) \cdot \Phi_\nu^3] dS, \\
 A_{0\nu\mu}^{12} &= \int_S [(\mathbf{n} \times \mathbf{N}_\mu^1) \cdot \Psi_\nu^3 + (\mathbf{n} \times \mathbf{M}_\mu^1) \cdot \Phi_\nu^3] dS, \\
 A_{0\nu\mu}^{21} &= \int_S [(\mathbf{n} \times \mathbf{M}_\mu^1) \cdot \Phi_\nu^3 + (\mathbf{n} \times \mathbf{N}_\mu^1) \cdot \Psi_\nu^3] dS, \\
 A_{0\nu\mu}^{22} &= \int_S [(\mathbf{n} \times \mathbf{N}_\mu^1) \cdot \Phi_\nu^3 + (\mathbf{n} \times \mathbf{M}_\mu^1) \cdot \Psi_\nu^3] dS,
 \end{aligned} \tag{30}$$

respectively. Here, M is the refractive index and is given by $M = \sqrt{\varepsilon_i/\varepsilon_s}$.

8 Acknowledgment

We would like to acknowledge support of this work by Deutsche Forschungsgemeinschaft (DFG).

9 Symbols and Abbriviations

a, b, c - bounds in x, y, z of the superellipsoid

(a_ν^0, b_ν^0) - expansion coefficients of the incident field

(a_ν^0, b_ν^0) - expansion coefficients of the incident field

D_{mn} -normalization constant

e - north-south roundedness of superellipsoid

$\mathbf{E}_0, \mathbf{E}_s$ - incident and scattered fields

(\mathbf{e}, \mathbf{h}) - surface current densities

(f_ν^0, g_ν^0) - expansion coefficients of the scattered field

k - wavenumber

$\{\mathbf{M}_{mn}^{1,3}, \mathbf{N}_{mn}^{1,3}\}$ - localized vector spherical functions

$\{\mathcal{M}_{mn}^{1,3}, \mathcal{N}_{mn}^{1,3}\}$ - distributed vector spherical functions

$\{\mathcal{M}_{ni}^{1,3}, \mathcal{N}_{ni}^{1,3}\}$ - magnetic and electric dipoles

$\{\mathcal{M}_n^{1,3}, \mathcal{N}_n^{1,3}\}$ - vector Mie-potentials

M - refractive index

n - east-west roundedness of superellipsoid

S - particle surface

$[\mathbf{T}]$ - transition matrix

(x, y, z) - cartesian coordinate

\mathbf{x} - position vector

$\alpha_n^\pm(\mathbf{x})$ - Green function

α, β, γ - Euler angles

(ϑ, φ) - angular coordinates

ϵ - permittivity

λ_0 -wavelength in vacuum

μ - permeability

v_i - vertex points on particle surface

References

- [1] T. Wriedt: A review of elastic light scattering theories. Part. Part. Syst. Charact. 15 (1998) 67-74.

- [2] A. R. Jones: Light scattering for particle characterization. *Progress in Energy and Combustion Science* 25 (1999) 1-53.
- [3] Bruce T. Draine, Piotr J. Flatau: Discrete-dipole approximation for scattering calculations. *Optical Society of America: Journal of the Optical Society of America / A.* 11 (1994) 1491-1499.
- [4] D.-P. Lin, H.-Y. Chen: Volume integral equation solution of extinction cross section by raindrops in the range 0.6-100 GHz. *IEEE transactions on antennas and propagation.* 49 (2001) 494-499.
- [5] W. Sun, Q. Fu, Z. Chen: Finite-difference time-domain solution of light-scattering by dielectric particles with a perfectly matched layer absorbing boundary condition. *Applied Optics* 38 (1999) 3141-3151.
- [6] Ping Yang, K. N. Liou, M. I. Mishchenko, Bo-Cai Gao: Efficient finite-difference time-domain scheme for light scattering by dielectric particles: application to aerosols. *Applied Optics* 39 (2000) 3727-3737.
- [7] P. W. Barber and S. C. Hill: *Light scattering by particles: computational methods* (World Scientific, Singapore,1990).
- [8] M. I. Mishchenko, L. D. Travis: Capabilities and limitations of a current FORTRAN implementation of the T-matrix method for randomly oriented, rotationally symmetric scatterers. *Journal of quantitative spectroscopy & radiative transfer.* 60 (1998) 309-324.
- [9] P. C. Waterman: New formulation of acoustic scattering. *J. Acoust. Soc. Am.* 45 (1969) 1417-1429.
- [10] P. C. Waterman: Symmetry, unitarity and geometry in electromagnetic scattering. *Physical Review D* 3 (1971) 825-839.
- [11] P. C. Waterman: Matrix formulation of electromagnetic scattering. *Proc. IEEE* 53 (1965) 805-812.
- [12] M. I. Mishchenko: Light scattering by randomly oriented axially symmetric particles. *J. Opt. Soc. Am. A* 8 (1991) 871-882.

- [13] B. Peterson and S. Ström: T-matrix for electromagnetic scattering from an arbitrary number of scatterers. *Physical Review D* 8 (1973) 3661-3678.
- [14] D. W. Mackowski: Calculations of total cross sections of multiple-sphere clusters. *J. Opt. Soc. Am. A* 11 (1994) 2851-2861.
- [15] D. Ngo, G. Videen and P. Chylek: A Fortran code for the scattering of EM waves by a sphere with a nonconcentric spherical inclusion. *Computer Physics Communications* 99 (1996) 94-112.
- [16] G. Videen, D. Ngo, P. Chylek, R. G. Pinnick: Light scattering from a sphere with an irregular inclusion. *J. Opt. Soc. Am. A* 12 (1995) 922-928.
- [17] Wenxin Zheng: The null-field approach to electromagnetic scattering from composite objects: The case with three or more constituents. *IEEE Trans. Antennas and Propagate.* 36 (1988) 1396-1400.
- [18] T. Wriedt, A. Doicu: Light scattering from a particle on or near a surface. *Optics Communications* 152 (1998) 376-384.
- [19] A. Boström: Scattering of acoustic waves by a layered elastic obstacle immersed in a fluid: An improved null-field approach. *J. Acoust. Soc. Am.* 76 (1984) 588-593.
- [20] M. F. Iskander, A. Lakhtakia, C. H. Durney: A new procedure for improving the solution stability and extending the frequency range of the EBCM. *IEEE Trans. Antennas Propag.* AP-31 (1983) 317-324.
- [21] M. F. Iskander, A. Lakhtakia: Extension of the iterative EBCM to calculate scattering by low-loss or loss-less elongated dielectric objects. *Appl. Opt.* 23 (1984) 948-953.
- [22] R. H. T. Bates, D. J. N. Wall: Null field approach to scalar diffraction: I General method; II Approximate methods; III Inverse methods. *Phil. Trans. Roy. Soc. London A* 287 (1977) 45-117.
- [23] A. Lakhtakia, M. F. Iskander, C. H. Durney: An iterative EBCM for solving the absorption characteristics of lossy dielectric objects of large aspect ratios. *IEEE Trans. Microwave Theory Tech.* MTT-31 (1983) 640-647.
- [24] R. H. Hackman: The transition matrix for acoustic and elastic wave scattering in prolate spheroidal coordinates. *J. Acoust. Soc. Am.* 75 (1984) 35-45.

- [25] F. M. Schulz, K. Stamnes, J. J. Stamnes: Scattering of electromagnetic waves by spheroidal particles: A novel approach exploiting the T-Matrix computed in spheroidal coordinates. *Applied Optics* 37 (1998) 7875-7896.
- [26] A. Doicu, T. Wriedt: EBCM with multipole sources located in the complex plane. *Optics communications* 139 (1997) 85-98.
- [27] T. Wriedt, A. Doicu: Formulations of the EBCM for three-dimensional scattering using the method of discrete sources. *Journal of Modern Optics* 45 (1998) 199-213.
- [28] A. Doicu, Y. Eremin, T. Wriedt: *Acoustic and Electromagnetic Scattering Analysis using Discrete Sources*. Academic Press, San Diego 2000.
- [29] A. Doicu, T. Wriedt: Extended boundary condition method with multipole sources located in the complex plane. *Optics Commun.* 139 (1997) 85-98.
- [30] A. Doicu, T. Wriedt: Null-field method with discrete sources to electromagnetic scattering from layered scatterers. *Comput. Phys. Commun.* 138 (2001) 136-142.
- [31] A. Doicu, T. Wriedt: Calculation of the T-matrix in the null-field method with discrete sources. *J. Opt. Soc. Am. A* 16 (1999) 2539-2544.
- [32] P. W. Barber: *Differential scattering of electromagnetic waves by homogeneous isotropic dielectric bodies*. Ph. D. Thesis, University of California, Los Angeles 1973.
- [33] J. B. Schneider, I. C. Peden: Differential Cross Section of a Dielectric Ellipsoid by the T-Matrix Extended Boundary Condition Method. *IEEE Trans. Antennas Propagat.* AP 36 (1978) 1317-1321.
- [34] T. Wriedt, A. Doicu: Formulations of the extended boundary condition method for three-dimensional scattering using the method of discrete sources. *Journal of modern optics* 45 (1998) 199-214.
- [35] T. Wriedt, U. Comberg: Comparison of Computational Scattering Methods. *J. Quant. Spectrosc. Radiat. Transfer* 60 (1998) 411-423.
- [36] H. Laitinen, K. Lumme: T-Matrix method for general star-shaped particles: first results. *J. Quant. Spectrosc. Radiat. Transfer* 60 (1998) 325-334.

- [37] F. M. Kahnert, J. J. Stannes, K. Stannes: Application of the extended boundary condition method to particles with sharp edges: a comparison of two surface integration approaches. *Applied Optics* *40* (2001) 3101-3109.
- [38] S. Havemann, A. J. Baran: Extension of T-matrix to scattering of electromagnetic plane waves by non-axisymmetric dielectric particles: application to hexagonal ice cylinders. *J. Quant. Spectrosc. Radiat. Transfer* *70* (2001) 139-158.
- [39] I. D. Faux, M. J. Pratt: Computational geometry for design and manufacture. Wiley & Sons, Chichester 1979.
- [40] A. Jaklic, A. Leonardis, F. Solina: Segmentation and recovery os Superquadratics. Kluwer Academic Publ. Dordrecht 2000.
- [41] C. Müller: Foundations of the mathematical theory of electromagnetic waves. Springer-Verlag, New-York, 1969.
- [42] J. Bloomenthal (ed.): Introduction to Implicit Surfaces. Morgan Kaufmann Publ., San Francisco, 1997.
- [43] A. Pasko: Function Representation and HyperFun Project. in Tosiyasu L. Kunii (Ed.): Proceedings of the 17th Spring Conference on Computer Graphics. 25th-28th April, 2001, Budmerice, Slovakia.
- [44] HyperFun Project: Language and Software for F-rep Modeling, URL: <http://www.hyperfun.org>.
- [45] A. Pasko, V. Adzhiev, A. Sourin, V. Savchenko, Function representation in geometric modeling: concepts, implementation and applications, *The Visual Computer* *11* (1995) 429-446.
- [46] K. Georg, J. Tausch: Some error estimares for the numerical approximation of surface integrals. *Math. Comp.* *62* (1994) 755-763.
- [47] T. Wriedt, A. Doicu: Formulation of the extended boundary condition method for three-dimensional scattering using the method of discrete sources. *Journal of Modern Optics* *45* (1998) 199-213.
- [48] Ch. Hafner, L. Bomholt: The 3D electromagnetic Wave Simulator, 3D MMP Software and User's Guide. Wiley, Chichester 1993.

- [49] Scott Hudson: The Earth-Crossing Asteroid 1998 KY26.
<http://www.eecs.wsu.edu/~hudson/Research/Asteroids/ky26/>
- [50] Roberto Cipolla, Peter Giblin: Visual motion of curves and surfaces. Cambridge University Press, Cambridge 2000.
- [51] POV ROCK gen 1.0 <http://www.iro.umontreal.ca/~pigeon/povpage/rockgen/rockgen.html>.
- [52] T. Wriedt: Electromagnetic scattering programs. <http://www.t-matrix.de>.

10 List of Figure Captions

Fig. 1: Examples of superellipsoids with parameters: $e = 0.2; 1.0; 1.0; 0.2; 2.0$ and $n = 0.2; 0.2; 1.0; 1.0; 2.0$. (left to right). $a = b = c = 1.0$.

Fig. 2: Form of rounded cubes used for computation $e = n = 0.2; 0.5; 0.7$ (left to right). In the examples the dimensions are $a = b = c = 0.3\mu m$ and the number of triangular patches are 1448, 1448, 1400.

Fig. 3: Differential scattering cross section of spheroid $a = b = 500nm, c = 700nm$, 10725 faces, $N_{\max} = 16, M_{\max} = 15, M = 1.5, \lambda = 628.31nm$.

Fig. 4: Orientation averaged differential scattering cross section of spheroid $a = b = 500nm, c = 700nm$, 10725 faces, 1000 orientations, $N_{\max} = 16, M_{\max} = 15, M = 1.5, \lambda = 628.31nm$.

Fig. 5: Differential scattering cross section of ellipsoid $a = 150, b = 200, c = 300nm$, 11656 faces, $64*64, M = 1.5, \lambda = 628.31nm, pol = 45^\circ, alpha = beta = 45^\circ$

Fig. 6: Differential scattering cross section (p polarization) of rounded cube with parameters $e = n = 0.2, a = b = c = 1000nm, N_{\max} = 20, M_{\max} = 18, M = 1.5, \lambda = 628.31nm$, DSM: 14648 faces; MMP 1/8 of cube with 1435 faces.

Fig. 7: Differential scattering cross section (s polarization) of rounded cube with parameters $e = n = 0.2, a = b = c = 1000nm, N_{\max} = 20, M_{\max} = 18, M = 1.5, \lambda = 628.31nm$, DSM: 14648 faces; MMP 1/8 of cube with 1435 faces.

Fig. 8: DSCS computed for convergence test versus number of integration points (faces) for a cube. $a = b = c = 300nm, n = e = 0.2, N_{\max} = 10, M_{\max} = 7, M = 1.5; \lambda = 628.31nm$.

Fig. 9: DSCS computed for convergence test versus number of expansion functions MN_{\max} for a cube $a = b = c = 1000nm, n = e = 0.5, faces = 14648, M = 1.5, \lambda = 628.31nm$.

Fig. 10: Differential scattering cross section (p polarization) of rounded cube with different values of e and n , $a = b = c = 1500nm$, $N_{\max} = 30$, $M_{\max} = 28$, 33464 faces, $M = 1.5$, $\lambda = 628.31nm$.

Fig. 11: Differential scattering cross section (s polarization) of rounded cube with different values of e and n , $a = b = c = 1500nm$, $N_{\max} = 30$, $M_{\max} = 28$, 33464 faces, $M = 1.5$, $\lambda = 628.31nm$.

Fig. 12: Differential scattering cross section (p polarization) of rounded cube with different values of e and n , $a = b = c = 2000nm$, $N_{\max} = 39$, $M_{\max} = 38$, 76220 faces, $M = 1.5$, $\lambda = 628.31nm$.

Fig. 13: Differential scattering cross section (s polarization) of rounded cube with different values of e and n , $a = b = c = 2000nm$, $N_{\max} = 39$, $M_{\max} = 38$, 76220 faces, $M = 1.5$, $\lambda = 628.31nm$.

Fig. 14: Orientation averaged differential scattering cross section of rounded cube with $e = n = 0.5$, $a = b = c = 2000nm$, $N_{\max} = 39$, $M_{\max} = 38$, 76220 faces, 2744 orientation, $M = 1.5$, $\lambda = 628.31nm$.

Fig. 15: Three views of ky26 shaped particle scaled down by $100\mu m/km$.

Fig. 16: Differential scattering cross section of ky26 shaped particle, $N_{\max} = 10$, $M_{\max} = 7$, 4092 faces, $M = 1.5$, $\lambda = 628.31nm$.

Fig. 17: Orientation averaged differential scattering cross section of ky26 shaped particle, 1000 orientations, $N_{\max} = 10$, $M_{\max} = 7$, 4092 faces, $M = 1.5$, $\lambda = 628.31nm$.

Fig. 18: Three views of “realistically” shaped particle.

Fig. 19: Orientation averaged differential scattering cross section of “real” shaped particle, 1728 orientations, $N_{\max} = 20$, $M_{\max} = 17$, 28032 faces, $M = 1.5$, $\lambda = 628.31nm$.

Fig. 20: Shape of smooth (left) and rough (right) particle.

Fig. 21: Orientation averaged differential scattering cross section of smooth and rough particle, 1728 orientations, $N_{\max} = 20$, $M_{\max} = 17$, 20480 faces, $M = 1.5$, $\lambda = 628.31nm$.

1 2 3 4 5 6

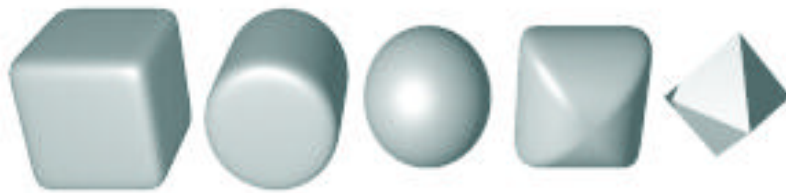


Fig. 1: Examples of superellipsoids with parameters: $e = 0.2; 1.0; 1.0; 0.2; 2.0$ and $n = 0.2; 0, 2; 1.0; 1.0; 2.0$. (left to right). $a = b = c = 1.0$.

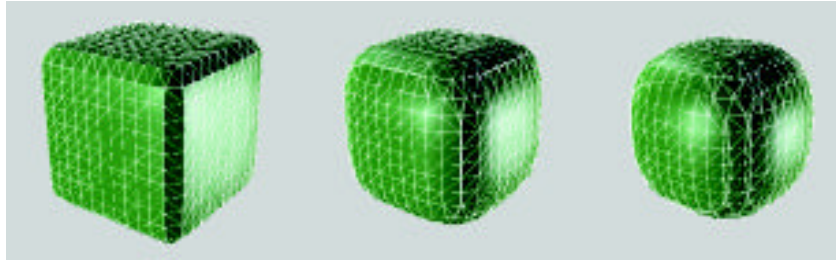


Fig. 2: Form of rounded cubes used for computation $e = n = 0.2; 0.5; 0.7$ (left to right). In the examples the dimensions are $a = b = c = 0.3\mu m$ and the number of triangular patches are 1448, 1448, 1400.

7

8

9 10

11 12 13 14 15 16 17 18 19

20 21

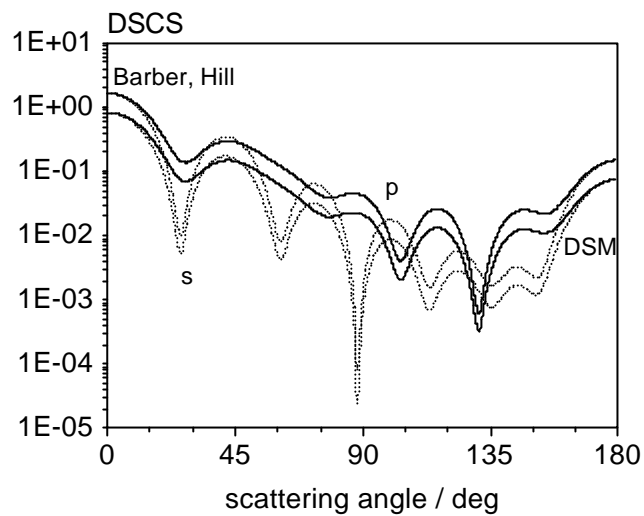


Fig. 3: Differential scattering cross section of spheroid $a = b = 500nm, c = 700nm$, 10725 faces, $N_{\max} = 16, M_{\max} = 15, M = 1.5, \lambda = 628.31nm$.

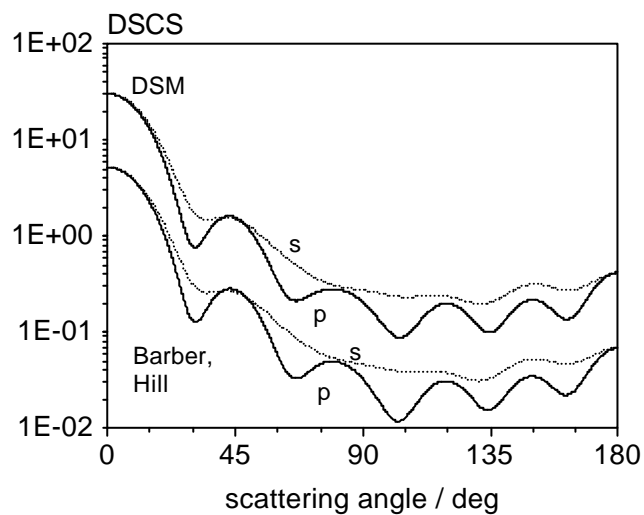


Fig. 4: Orientation averaged differential scattering cross section of spheroid $a = b = 500nm, c = 700nm$, 10725 faces, 1000 orientations, $N_{\max} = 16, M_{\max} = 15, M = 1.5, \lambda = 628.31nm$.

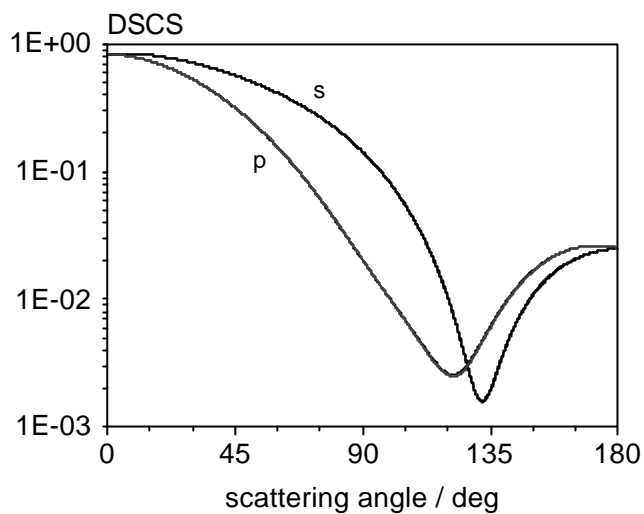


Fig. 5: Differential scattering cross section of ellipsoid $a = 150, b = 200, c = 300nm$, 11656 faces, $64*64$, $M = 1.5$, $\lambda = 628.31nm$, $pol = 45^\circ$, $alpha = beta = 45^\circ$

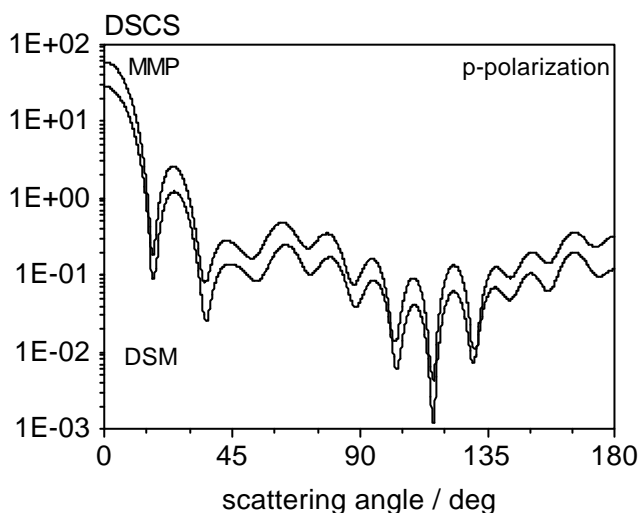


Fig. 6: Differential scattering cross section (p polarization) of rounded cube with parameters $e = n = 0.2, a = b = c = 1000nm$, $N_{max} = 20, M_{max} = 18, M = 1.5, \lambda = 628.31nm$, DSM: 14648 faces; MMP 1/8 of cube with 1435 faces.

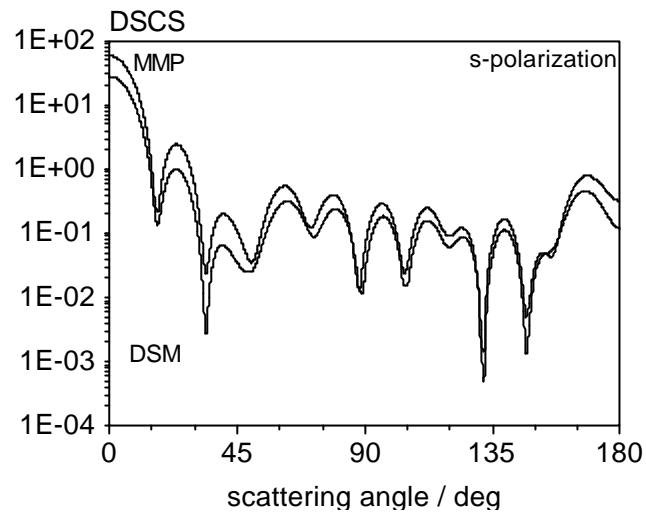


Fig. 7: Differential scattering cross section (s polarization) of rounded cube with parameters $e = n = 0.2$, $a = b = c = 1000nm$, $N_{\max} = 20$, $M_{\max} = 18$, $M = 1.5$, $\lambda = 628.31nm$, DSM: 14648 faces; MMP 1/8 of cube with 1435 faces.

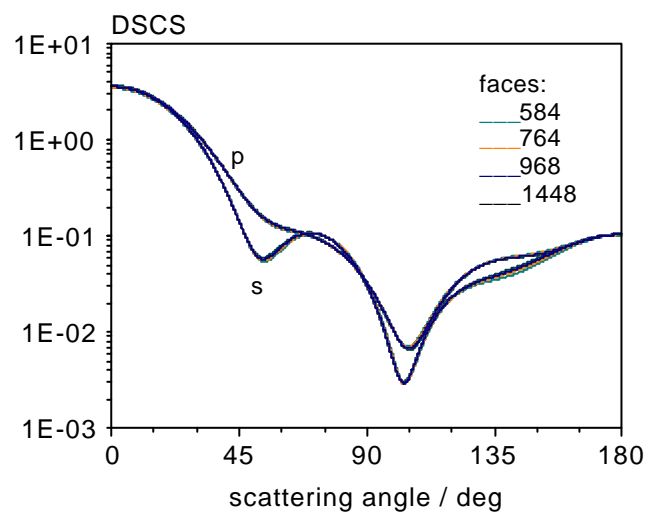


Fig. 8: DSCS computed for convergence test versus number of integration points (faces) for a cube $a = b = c = 300nm$, $n = e = 0.2$, $N_{\max} = 10$, $M_{\max} = 7$, $M = 1.5$; $\lambda = 628.31nm$

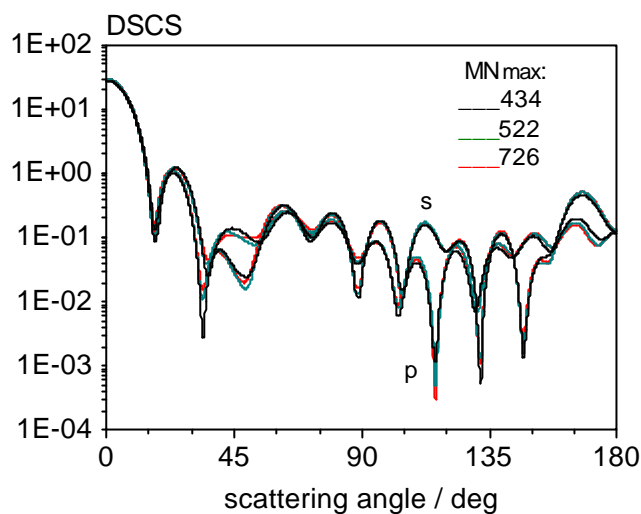


Fig. 9: DSCS computed for convergence test versus number of expansion functions N_{\max} for a cube $a = b = c = 1000nm$, $n = e = 0.5$, faces = 14648, $M = 1.5$, $\lambda = 628.31nm$

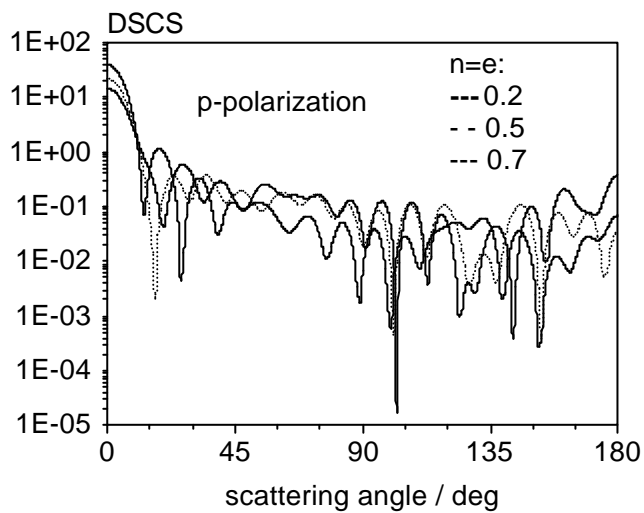


Fig. 10: Differential scattering cross section (p polarization) of rounded cube with different values of e and n , $a = b = c = 1500nm$, $N_{\max} = 30$, $M_{\max} = 28$, 33464 faces, $M = 1.5$, $\lambda = 628.31nm$.

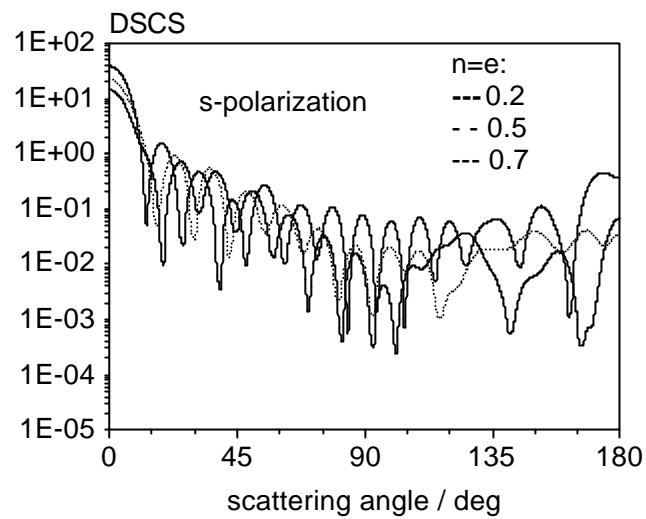


Fig. 11: Differential scattering cross section (s polarization) of rounded cube with different values of e and n , $a = b = c = 1500nm$, $N_{\max} = 30$, $M_{\max} = 28$, 33464 faces, $M = 1.5$, $\lambda = 628.31nm$.

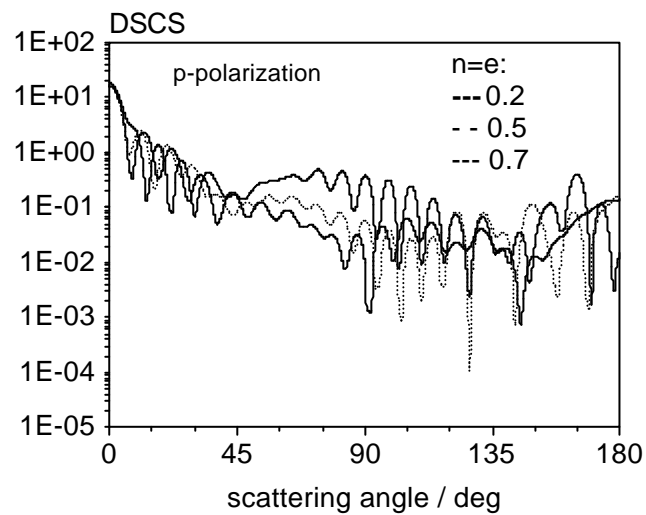


Fig. 12: Differential scattering cross section (p polarization) of rounded cube with different values of e and n , $a = b = c = 2000nm$, $N_{\max} = 39$, $M_{\max} = 38$, 76220 faces, $M = 1.5$, $\lambda = 628.31nm$.

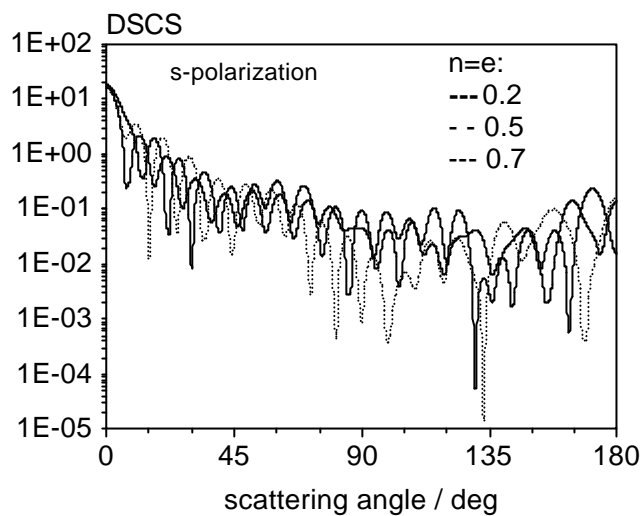


Fig. 13: Differential scattering cross section (s polarization) of rounded cube with different values of e and n , $a = b = c = 2000nm$, $N_{\max} = 39$, $M_{\max} = 38$, 76220 faces, $M = 1.5$, $\lambda = 628.31nm$.

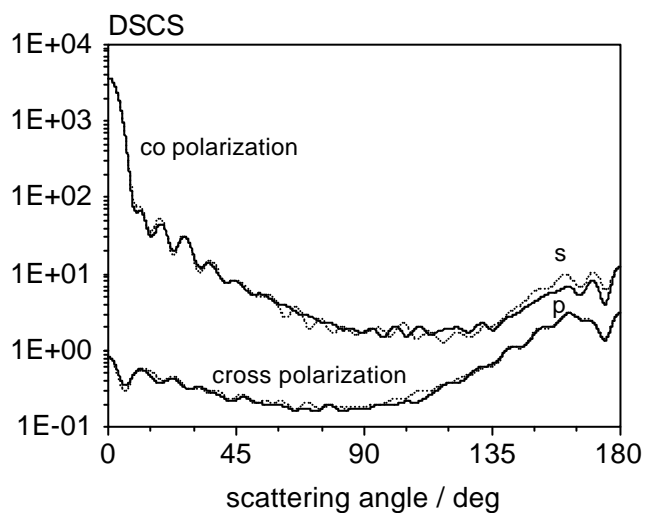


Fig. 14: Orientation averaged differential scattering cross section of rounded cube with $e = n = 0.5$, $a = b = c = 2000nm$, $N_{\max} = 39$, $M_{\max} = 38$, 76220 faces, 2744 orientation, $M = 1.5$, $\lambda = 628.31nm$.

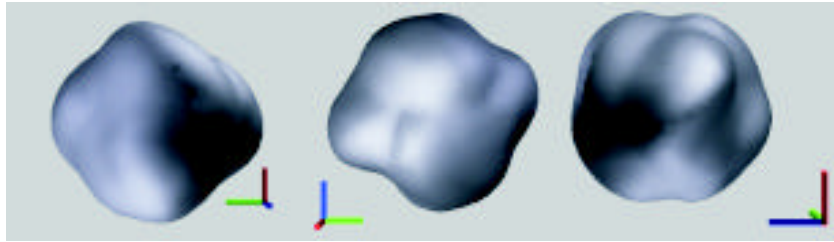


Fig. 15: Three views of ky26 shaped particle scaled down by $100\mu\text{m}/\text{km}$.

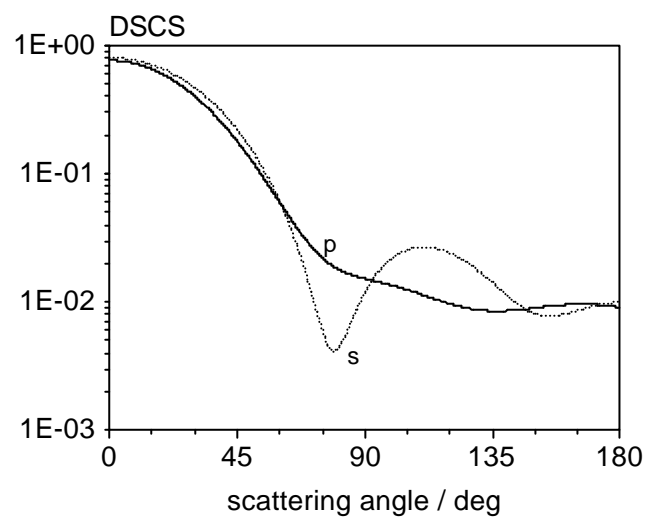


Fig. 16: Differential scattering cross section of ky26 shaped particle, $N_{\text{max}} = 10$, $M_{\text{max}} = 7$, 4092 faces, $M = 1.5$, $\lambda = 628.31\text{nm}$.

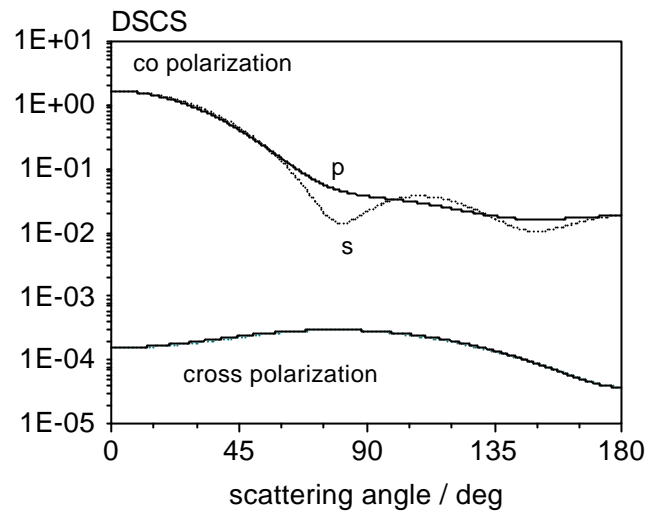


Fig. 17: Orientation averaged differential scattering cross section of ky26 shaped particle, 1000 orientations, $N_{\max} = 10$, $M_{\max} = 7$, 4092 faces, $M = 1.5$, $\lambda = 628.31nm$.

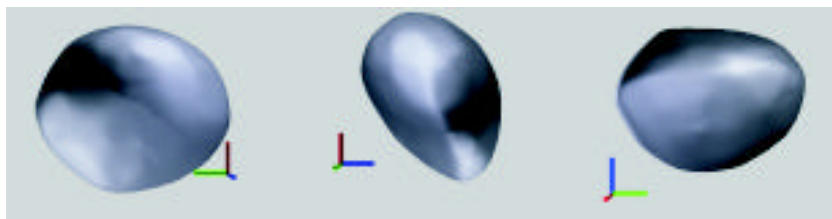


Fig. 18: Three views of “realistically” shaped particle.

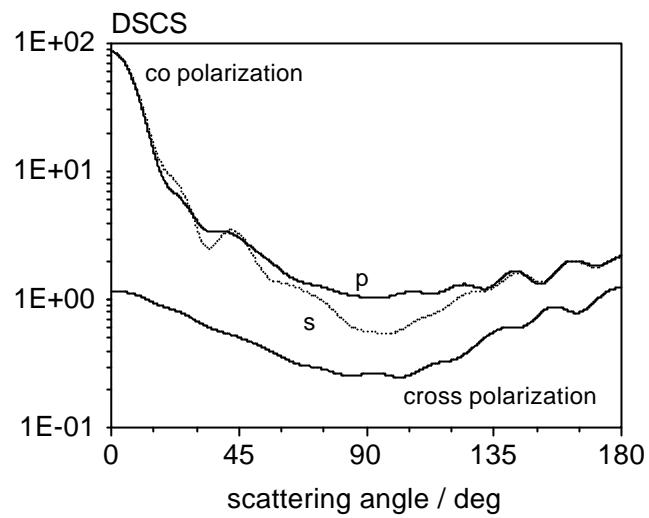


Fig. 19: Orientation averaged differential scattering cross section of “real” shaped particle, 1728 orientations, $N_{\max} = 20$, $M_{\max} = 17$, 28032 faces, $M = 1.5$, $\lambda=628.31\text{nm}$.

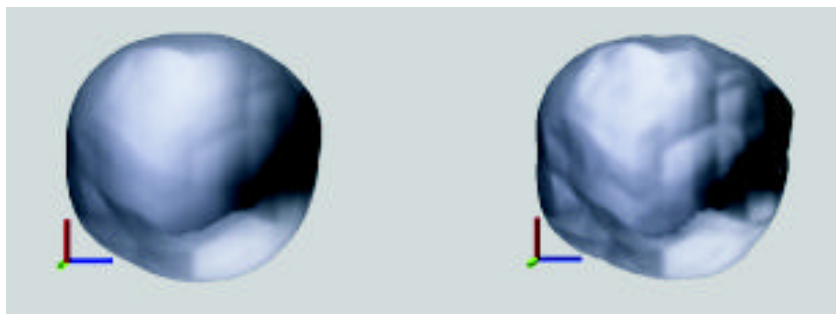


Fig. 20: Shape of smooth (left) and rough (right) particle.

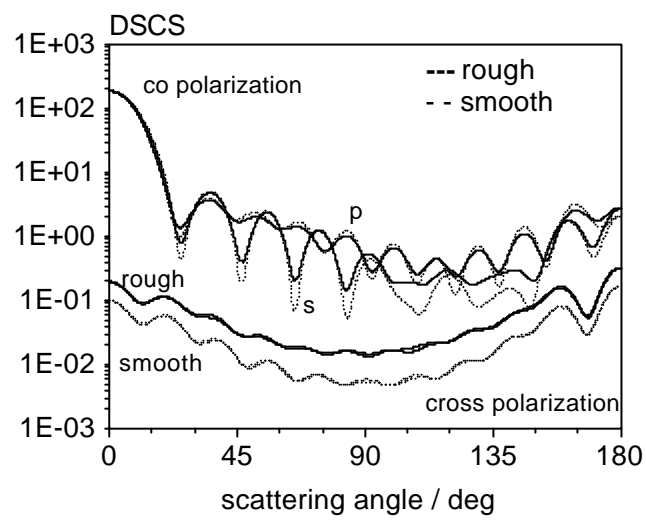


Fig. 21: Orientation averaged differential scattering cross section of smooth and rough particle, 1728 orientations, $N_{\max} = 20$, $M_{\max} = 17$, 20480 faces, $M = 1.5$, $\lambda = 628.31nm$.